



Cold sintering process of hydroxyapatite derived from natural bone and co-precipitation method: a comparative study



Hawraa O. Abbas ^{a*}, Hanaa A. Smeig ^a, Zuhair J. Abdul Ameer ^b

^a Materials Engineering Dept., University of Technology-Iraq, Alsina'a street, 10066 Baghdad, Iraq.

^b Prosthetics and Orthotics Engineering Dept., College of Engineering, Kerbala University, Iraq.

*Corresponding author Email: Hawraaoday1992@gmail.com

HIGHLIGHTS

- A novel cold sintering process produced highly dense hydroxyapatite (HA) samples.
- Nano-HA was prepared via two routes: bovine bone (HA₁) and chemical precipitation (HA₂).
- The difference in cold sintering between the HA₁ and HA₂ powders is explained.
- Cold sintering yielded high density, purity, and stability HA without thermal decomposition.
- Structural, morphological, mechanical and physical properties of the compact samples were studied

ARTICLE INFO

Handling editor: Akram R. Jabur

Keywords:

Cold sintering process; Boven bone; nano-hydroxyapatite; Densification; chemical precipitation method.

ABSTRACT

This study uses a novel sintering technique at very low temperatures (below 300°C) named the Cold Sintering Process to produce highly dense Hydroxyapatite (HA) samples. Nano hydroxyapatite was prepared using two different methods: Synthesis by chemical precipitation method (HA₁) and natural source from Boven bone (HA₂). The samples are characterized using scanning electron microscope (SEM), X-ray energy dispersive spectrometry (EDS), X-ray diffractogram (XRD), transition electron microscope (TEM), Fourier transform infrared spectrometry (FTIR) and Nuclear magnetic resonance spectroscopy (NMR). Also, physical and mechanical properties measurements were detected, including density and hardness. The results indicated that cold sintering could result in Hydroxyapatite with high densification, high purity, and high stability without thermal decomposition compared with traditional sintering. The relative density and hardness for HA₁ are 99% and 502HV, respectively. The relative density and hardness for HA₂ are 69% and 350HV, respectively. It can be observed that the HA₁ sample has higher densification than HA₂ due to the presence of organic matter in natural Hydroxyapatite HA₂. This organic material will be removed during the cold sintering process, leaving pores that lead to low densification of HA₂ samples. It can be concluded that the synthesis hydroxyapatite (HA₁) can be easily sintered by a cold sintering process compared with natural one(HA₂).

1. Introduction

The skeletal system, composed of bones, joints, and teeth, can recover from various injuries with minimal medical intervention. However, since man entered the industrial era, orthopedic accidents produced more complex injuries. In certain cases, orthopedic surgery is required to rebuild or replace the damaged bone [1].

Nonstoichiometric Hydroxyapatite (HA) is a bone mineral component that provides stiffness and appropriate mechanical properties. Natural apatites are observed in bones and pathologic tissue, such as mineralized soft tissue, teeth, and urolithi [1]. Hydroxyapatite is an interesting option for replacement bones because of its structural and chemical analogy to bone minerals. Hydroxyapatite is a bioactive (direct bonding with living tissue) and a biocompatible, non-immunogenic agent, non-inflammatory, non-toxic, and osteoconductive [2]. Hydroxyapatite (Ca₁₀(PO₄)₆OH₂) can be observed by several synthetic methods and by natural sources (extracted human teeth, bovine bone, pig teeth and bones, and cuttlefish) [3,4]

Hydroxyapatite needs a temperature of more than 1200°C for densification during conventional sintering. The high temperatures sintering consume energy and time. On the other hand, it decreases HA's biological activity, deteriorates its structural stability, and causes loss of the hydroxyl group [4]. Several methods are used to solve this problem, including sintering HA at low temperatures, such as spark plasma sintering (SPS), to consolidate the initial powder in an inert atmosphere at temperatures less than 300°C while retaining its bioactivity [5]. Recently, Guo et al. [6-11] showed that many ceramics could be

sintered and densified at temperatures between 20 and 300°C when pressure was applied, and they called this procedure the cold sintering process (CSP). In CSP, the initial powder is mixed with a solvent that partially dissolves the particles to facilitate the mass transport of powders at low temperatures under a uniaxial pressure [7]. The cold sintering process (CSP) is used for sintering numerous ceramics and composite materials made from extremely different materials, like polymer/ceramics [12-22]. However, Hassan and Ryu have recently reported the synthesis of high-density iodine-substituted Hydroxyapatite without adding any solvent via CSP, which obviously does not conform to the classical dissolution–precipitation mechanism. Nevertheless, they did not pay attention to this important issue [4].

Ping Shen et al. employed several commercial HA powders and sintered them via a cold sintering process for comparison. Several factors are studied, including temperature, pressure, and type of solvents (deionized water, ammonium hydroxide (14 M), and acetic acid solution (1 M)). Only the HA Prepared by the co-precipitation method can achieve high density with a relative value of over 90%, which is generally consistent with the finding of Hassan and Ryu [9].

Jong-Il Yun et al. used a cold sintering route to consolidate silica-incorporated Hydroxyapatite (Si-HAp) composite at 200 °C by applying a uniaxial pressure of 500 MPa for a short holding time. The higher relative sintered density of up to 98.0% was achieved by 25 wt% Si-loaded Hap [23].

This work used two main sources to prepare Hydroxyapatite's initial powder: a chemically precipitated method and a natural source (Boven bone). The natural source (Boven bone) was the first to sinter via the Cold Sintering Process (CSP). Two types of hydroxyapatites were sintered by CSP using an aqueous dissolution (deionized water) and the structural and morphological properties. This work aimed to study the difference between the CSP of two powders (HA₁&HA₂). The influence of different factors (temperatures, pressures, holding time, powder type, and liquid contents) on the relative density of HA₁ and HA₂ are studied in our work.

2. Materials and methods

2.1 Materials

Calcium nitrate tetrahydrate [Ca(NO₃)₂·4H₂O, Fluka, NLT 99%], diammonium hydrogen phosphate [(NH₄)₂HPO₄, Fluka, NLT 99%], ammonium hydroxide solution [NH₄OH, Fluka, Min. 28%].

2.2 Synthesis of Nano-HA by chemical precipitation method

Nano-HA1 powders used in this work were mainly synthesized via the chemical precipitation method [2], as shown in Figure 1. By dissolving the desired amount of diammonium hydrogen phosphate (DAP, 0.100M) and calcium nitrate (CN, 0.167 M) in double distilled water at 25°C using magnetically stirring for 45 min. A digital pH meter (Systronics 335, India) was used to measure the pH of the prepared solutions. Concentrated NH₄OH was used to adjust the pH of these solutions to 10.5-11 in whole experiments—several factors affect hydroxyapatite nano powders' formation by chemical precipitation methods. The most important one is that the PH value of the starting solutions must be basic to get phase purity and stability without thermal decomposition. The Base-Base reaction gives higher crystallinity than the Acid-Base reaction, indicating that the basic media is more favorable to forming HA nanoparticles. This is because the kinetics of ACP transformation to HA increase rapidly at pH > 10. With continuous stirring, 100 ml of the CN solution was slowly added dropwise to 100 ml of the APH solution. The white precipitate was subjected to aqueous washes followed by methanol washes after aging for a specific duration at 25°C. The resulting gel was oven-dried in the air at 100°C.

2.3 Extraction of HA from bovine bone by thermal decomposition

This study used a sufficient quantity of biowaste bovine femur bone to extract Hydroxyapatite. The bone first underwent a deproteinization procedure to remove the organic matter (tissue, marrow) from the bovine bone [2]. Figure 2, schematics illustrate the “degriasing, deproteinization and pulverizing treatments of Bovine bone.” First, the collected bones were first cleaned from the meat using a knife, then boiled using a domestic stainless steel pressure cooker with deionized water covering the bone for fat removal. The bones were washed, dried in a 100°C oven, and broken into fragments with a pestle and mortar. Then, the powder was ground for 6 hours at a speed of 400 rpm in a planetary ball mill. Lastly, the ground powder is sieved to obtain the desired particle size fraction.

2.4 Cold Sintering Process

The most important production parameters are their levels (Cold sintering temperature°C), Pressure (MPa), Holding time (min), and liquid content (wt%)) necessary to produce dense HA₁ and HA₂. A desired amount of the liquid phases was mixed with the separated HA₁ and HA₂ powder manually in a pestle and mortar for 3 minutes. After mixing, 1 g was put into a cylindrical stainless-steel die with a diameter of 12.88 mm. A uniaxial pressure was increased gradually to the desired value using a manual hydraulic press. The pressing was achieved at room temperature by a hand-made experimental setup containing (an iron frame, heater, temperature controller, variac, manual hydraulic press, and a thermocouple) as illustrated in Figure 3. The experimental setup is similar to the setup of the following work [11,14-15]

The tolerance between the die and plunger allowed liquid penetration; thus, all the extra liquid flows out under pressure. Within a few minutes, the temperature increases from ambient temperature to the desired temperature at a constant rate of 5°C/min. The temperature was kept constant for the desired time, and then the pressure was released with the cooling down to prepare disk-like samples with approximately 12.88 mm in diameter and around 5 mm in height. The procedure for sample preparation is summarized in Figure 3.

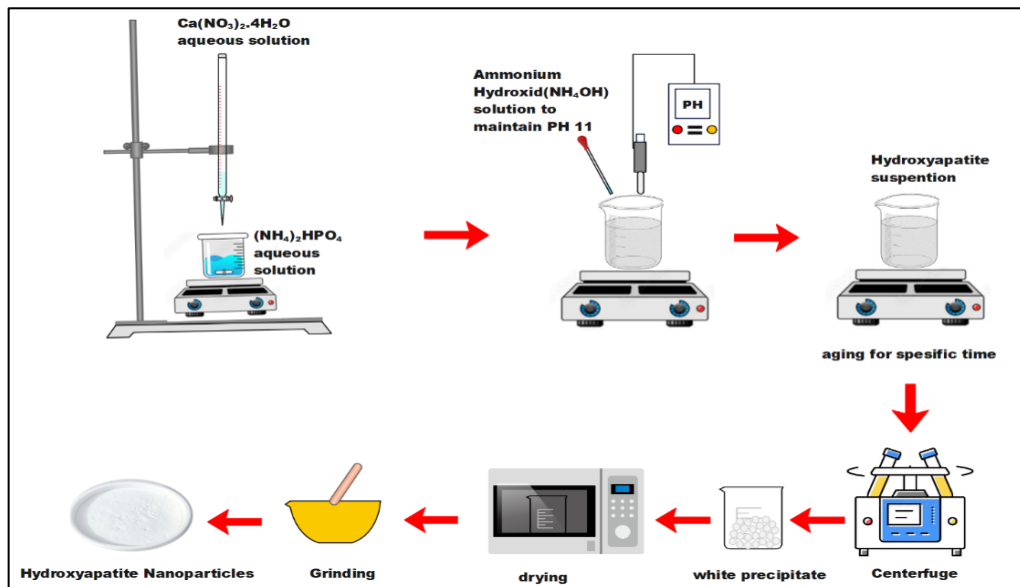


Figure 1: Schematic illustrating the co-precipitation method for preparing Nano-Hydroxyapatite (HA₁)

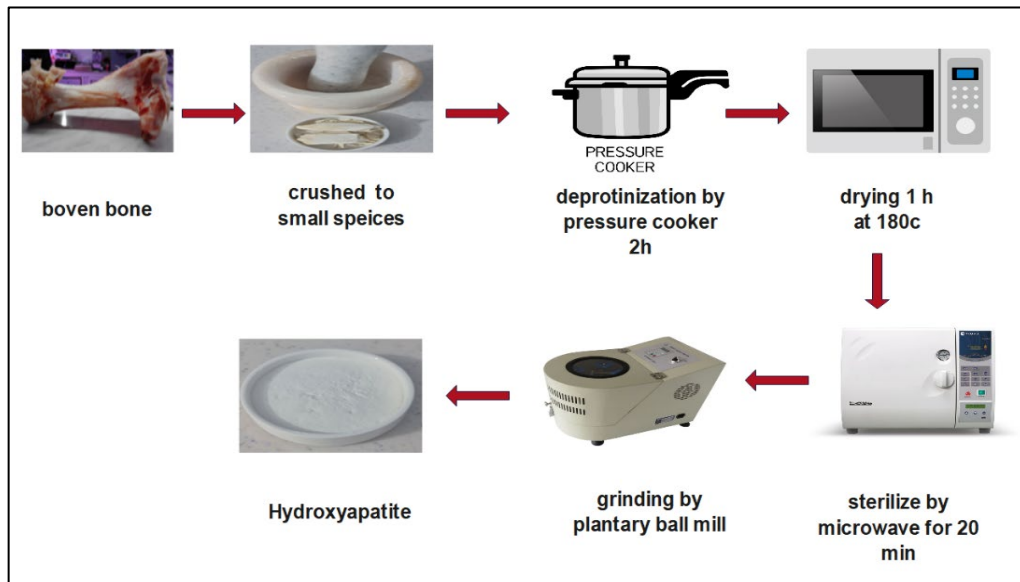


Figure 2: Schematic illustrating the steps for preparing Nano-Hydroxyapatite (HA₂) from natural sources

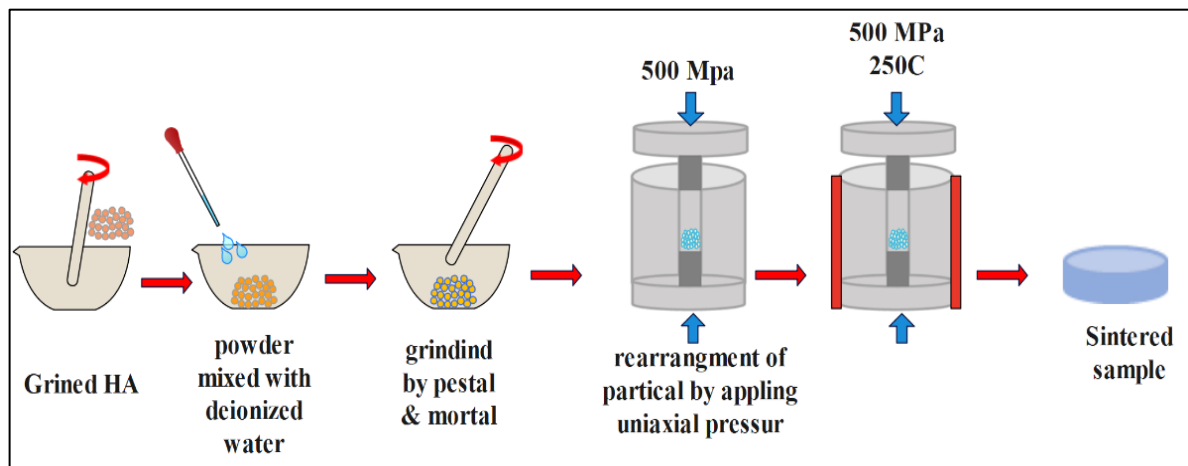


Figure 3: Schematic illustrates the procedure for preparing a compact of HA by cold sintering process (CSP)

2.5 Chemical and morphological characterization

Functional groups of the prepared nano HA powders and nano HA-PEEK composites were identified by Fourier transform infrared spectrometry (FT-IR, Magna-IR 750, Nicolet, USA). The spectra were recorded from 4000 cm^{-1} to 400 cm^{-1} . X-ray

diffraction (XRD, Shimadzu, Japan) using a Cu target examines the crystalline phases of nano HA powders sintered samples. The diffraction angles (2θ) were set between 10 and 60. Phases were identified by comparing the sample diffraction pattern with reference cards from the ICDD-JCPDS database.

A field emission scanning electron microscope (FE-SEM, JSM-6701F, JEOL, Tokyo, Japan) is used to characterize the surface morphology of the sintered samples. Before FE-SEM observation, All samples were coated with gold for 1 minute. Energy dispersive X-ray spectroscopy (EDS) was also recorded using the same equipment to confirm the element in the prepared sample.

“Thermogravimetric analysis (TGA) of the HA₁ and HA₂ was performed under inert gas (N₂) in the temperature range of 30–750°C at a heating rate of 10°C/min using the Labsys Evo-gas option (SETARAM). ¹H and ³¹P solid-state Nuclear magnetic resonance (NMR) spectra were obtained using an Agilent 400 MHz 54 mm NMR DD2 operating at 9.39 T, 161.82 MHz, 600 s to identify and confirm the presence of HPO₄²⁻ and H₂O on the surface of the HA₁ and HA₂ nanocrystals”.

2.6 Mechanical Properties

Vickers microhardness (HV) was also tested using Shimadzu Microhardness Tester (HMV-2L). A force (P) with a 1.961 N load and 15 s dwell time to obtain an indentation with crack propagation. Six points were chosen and measured in different positions of each sample to get an average value.

2.7 Physical Properties

Archimedes' principle, as described in the ASTM B 311-08 standard, was used to calculate all sample densities using the following formula:

$$RD = \frac{\rho}{\rho_k} \times 100 \quad (1)$$

where RD = Relative density (%); ρ = “Experimentally measured density (g/cm³)”; ρ_k = “Theoretical density calculated based on powder mixture ratios (g/cm³)”, the theoretical density of HA is 3.219 g/cm³”.

3. Results and Discussion

3.1 Physical Tests Results

Figure 5 explains the variations of relative density of HA₁ & HA₂ versus cold sintering parameters: (a) liquid content, (b) holding time, (c) pressure, (d) temperature, and (e) powder types. The optimal sample of HA₁ and HA₂, the hardest and densest, is prepared under a sintering temperature of 250°C, sintering pressure of 500 MPa, holding time of 60 min, and liquid content of 10 wt.% as shown in Figure 5a. The relative density and hardness for HA₁ are 99% and 502HV, respectively. The relative density and hardness for HA₂ are 69% and 350HV, respectively. It can be observed that the HA₁ sample has higher densification than HA₂ due to the presence of organic matter in natural Hydroxyapatite HA₂. This organic material will be removed during the cold sintering process, leaving pores that lead to low densification of HA₂ samples. It can be concluded that the synthesis hydroxyapatite (HA₁) can be easily sintered by a cold sintering process compared with natural one (HA₂).

To explain the densification mechanism of Hydroxyapatite during the cold sintering process and to explain the effects of each cold sintering factor, the following paragraph as shown in Figure 4. At the apatite nanocrystals' surface, water exists as a hydrated layer (adsorbed water), called an amorphous layer of chemisorbed and physisorbed water [12]. Under 500 MPa applied pressure Figure 5d, during the earliest stages of sintering, the highest densification was achieved by Breaking soft agglomerates of HA particles. The amorphous layer may be trapped between the solid-solid interfaces, which helps the HA particles slide and rearrange [4]. In this study, the system utilized is an open system from a thermodynamic view. When the temperature is applied, the amorphous phase becomes supersaturated, resulting in partial dehydration in the absorbed water of the amorphous layer. The electrostatic forces induced by the elimination of the adsorbed water can further strengthen the bond of the partly dehydrated HA surface [24] when the sintering temperatures reach higher than 250°C Figure 5c, resulting in residual porosity and decreasing density because of the excessive removal of amorphous layers adsorbed.

After 60 minutes of holding time Figure 5b, the highest possible sintered density of 99% was achieved for HA₁ and 69% for HA₂. Depending on the sintered materials, an appropriate holding period of 30 to 60 minutes is required to allow the HA particles coalescence and densification under pressure while the absorbed water is slowly released. Mass movement and the fusion of tiny crystallites at a slow heating rate of 20°C/min could promote complete compaction with the rearrangement of the solid-solid interfaces [15]. The amount of water present significantly impacts the cold sintering process. The densification is achieved at a 10% weight percentage of liquid content as shown in Figure 5a due to the increased amorphousness of the HA₁ surfaces, resulting in maximum densification (99% relative density) higher than the relative density prepared by [5,10-11].

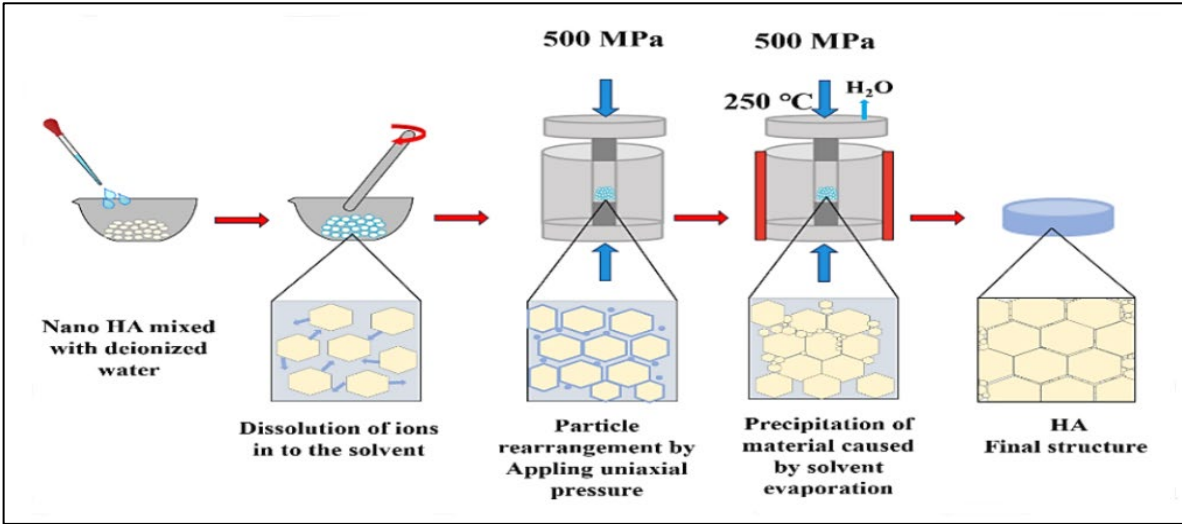


Figure 4: Schematic illustrating the mechanism of hydroxyapatite densification during the cold sintering process

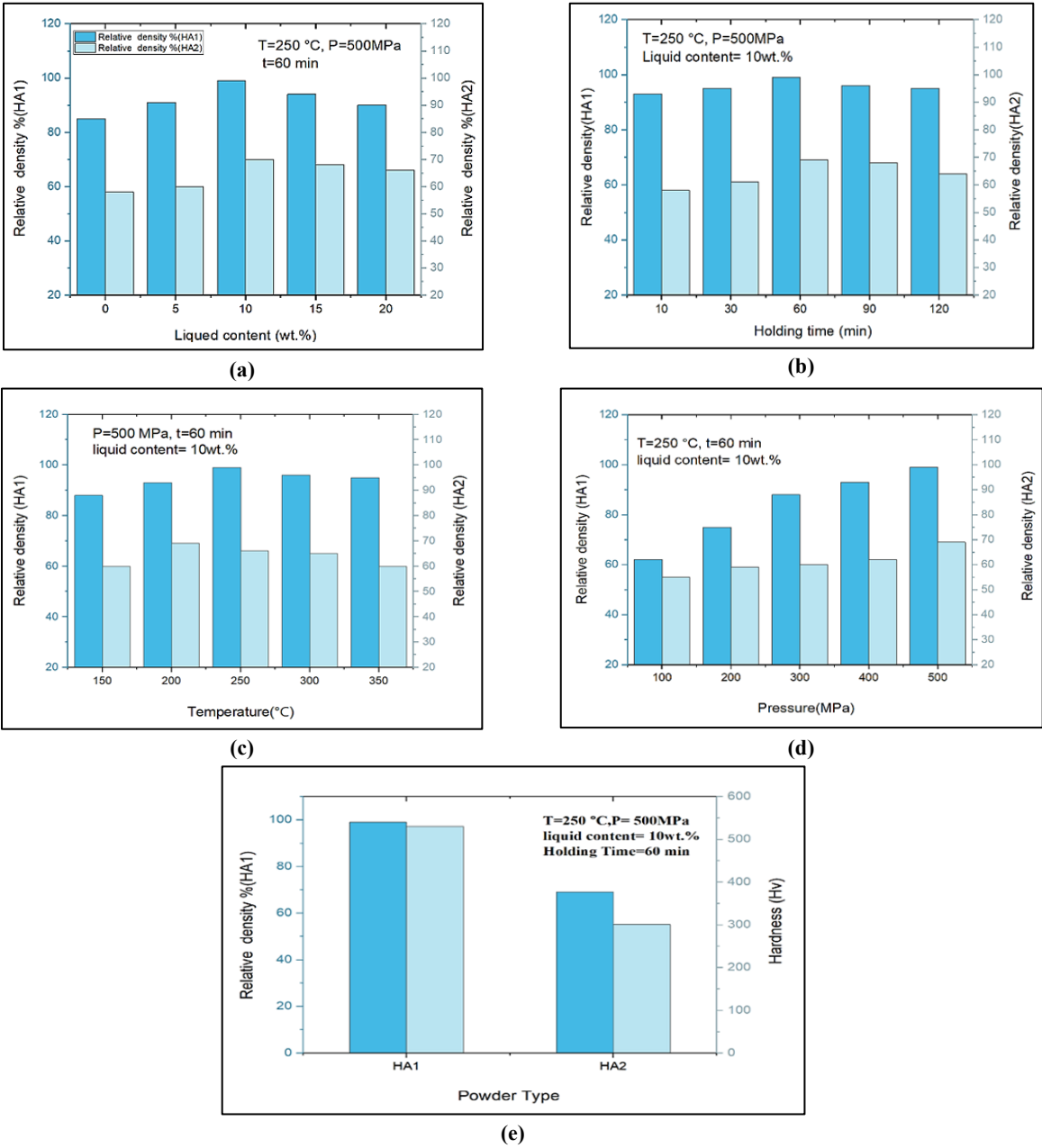


Figure 5: The variations of relative density of HA1 &HA2 versus cold sintering parameters: (a) liquid content, (b) holding time, (c) pressure, (d) temperature, and (e) powder types

3.2 TEM Results

TEM observed morphologies of the obtained HA₁ Figure 6 a,b and HA₂ Figure 6 c,d nanocrystals. Figure.6 showed an aggregate of nanoparticles with different c/a ratios, all having a size of less than 100 nm, which is generally consistent with the findings of Hassan and Ryu [4]. The average crystallite sizes, calculated using the Image J program as shown in Figure 7a for HA₁ and Figure 7b for HA₂, were 17 nm and 32 nm for HA₁ and HA₂, respectively. Pure HA nanoparticles strongly tended to form agglomerates due to their high surface area and surface energy.

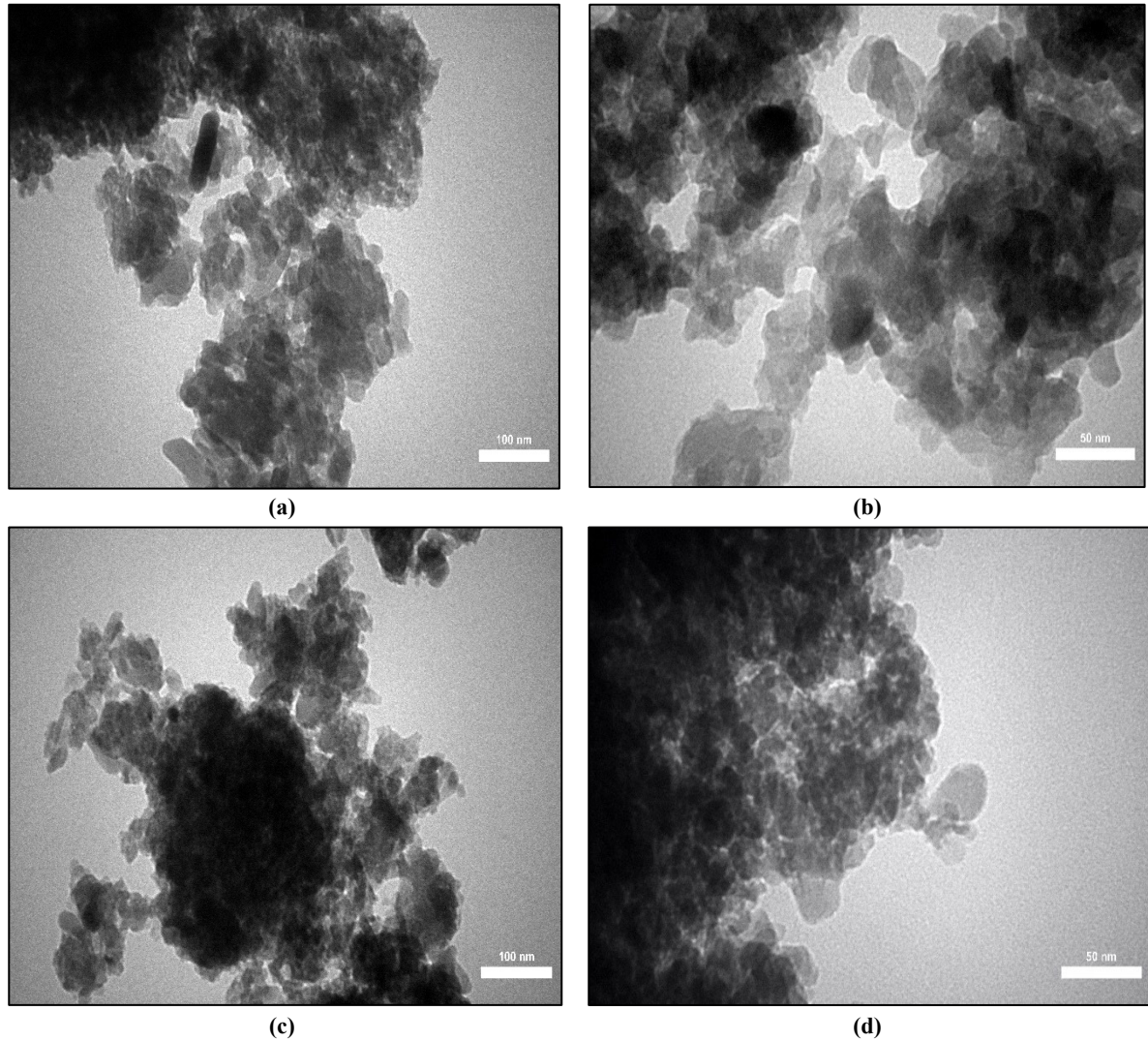


Figure 6: TEM results of the prepared Hydroxyapatite HA₁ (a,b) and powder HA₂ (c,d)

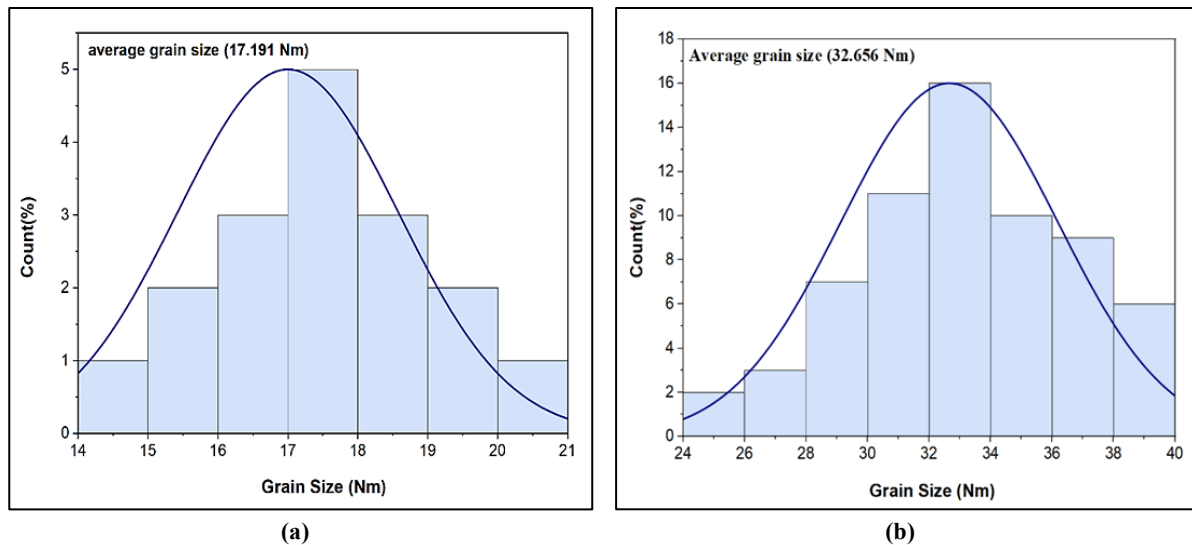


Figure 7: Average grain size for (a) HA₁ and (b) HA₂

3.3 Brunauer, emmett, and teller (BET) surface area analysis

Figure 8 a shows the plots of adsorption and desorption isotherms of the prepared HA₁ sample. The profile of these plots matches with 'type II' of the six principal classes of isotherm shapes describing nonporous solids' adsorption [14]. As expected, the estimated particle size fully agrees with the TEM observations. As Figure 8 b the synthesized's average particle size and BET surface area were 19 nm and 107 m²/g, respectively.

3.4 Thermal Analysis Results

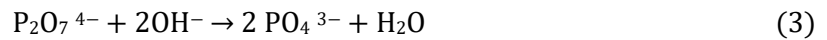
Figure 9 a and b shows the TGA and DTGA thermograms of prepared HA₁&HA₂ samples. During the heating, different weight loss stages are distinguished on the thermograms by dashed lines, and each step has been given a number.

First, at a temperature of 200°C, the weight loss corresponds to removing physically absorbed water. Next, above 200°C, the weight loss corresponds to the chemisorbed water and carbonate loss. Reyes-Gasga et al., [15]. They reached a similar conclusion in their TG analysis of the co-precipitated Hydroxyapatite.

The decomposition of HPO₄²⁻ occurs in the temperatures between 200°C up to 650°C according to the reaction [16]:



As reported by Lee et al. [17], when the temperature Increased above 700°C, P₂O₇⁴⁻ and OH⁻ ion might have reacted to form PO₄³⁻ and H₂O, according to the reaction:



Eventually, the weight loss continuously occurs up to 850°C, corresponding to adsorbed H₂O in the powders and interstitial water in the structure. The total mass loss in the samples HA₁ is about 10%.

In the case of bovine bone (HA₂), the results clearly show that different temperatures led to varying levels of organic matter removal. Water and organic matter were removed at temperatures of 100°C and 350°C. No noticeable weight loss was observed at a temperature above 700°C. All organic issues like lipids, collagen, keratin sulphate, and chondroitin sulphate were eliminated below 700°C.

3.5 NMR Results

Nuclear magnetic resonance spectroscopy(NMR) is well known that HA nanopowders made by chemical precipitation Figure10 a and b and Boven bone Figure10 c and d have crystalline and amorphous phases. These results are in agreement with the previous research, which supports the coexistence of these two phases and shows an amorphous phase exists on the nanocrystal surface of HA₂ [20-22] and HA₁ [5] [25-29]. The majority of the amorphous, non-apatitic portion is made up of ionic species such as Ca²⁺, HPO₄²⁻, CO₃²⁻, and H₂O. The HPO₄²⁻ and OH ions concentration in the amorphous part of the synthesized nanocrystals can rise in any adsorbed water on their surface [21]. Amorphous phase and water were confirmed in the solid-state NMR data of the HA samples. Figure 10 a. Shows the ¹H signal, which is divided into two parts: a narrow signal at about 0 ppm and a broad signal from 3 to 15 ppm. The wide signal showed that H₂O and HPO₄²⁻, were on the nanocrystals as amorphous layers. Figure 10 b Displays the ³¹P signal from the HA samples typically indicates apatitic phosphates.

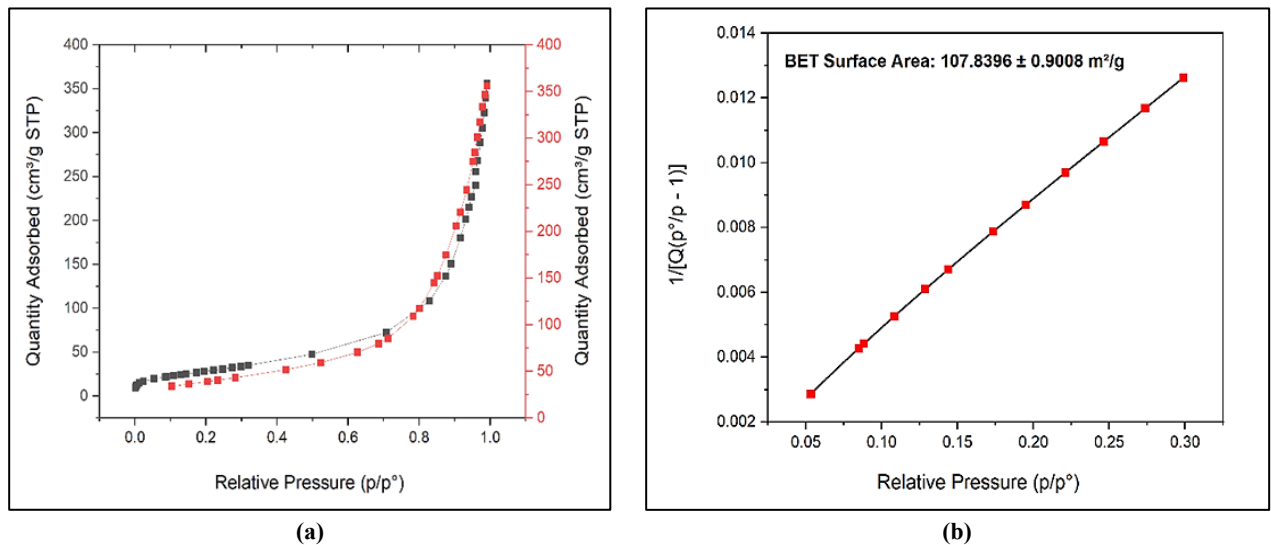


Figure 8: Plots of adsorption and desorption isotherms of the prepared HA₁ sample

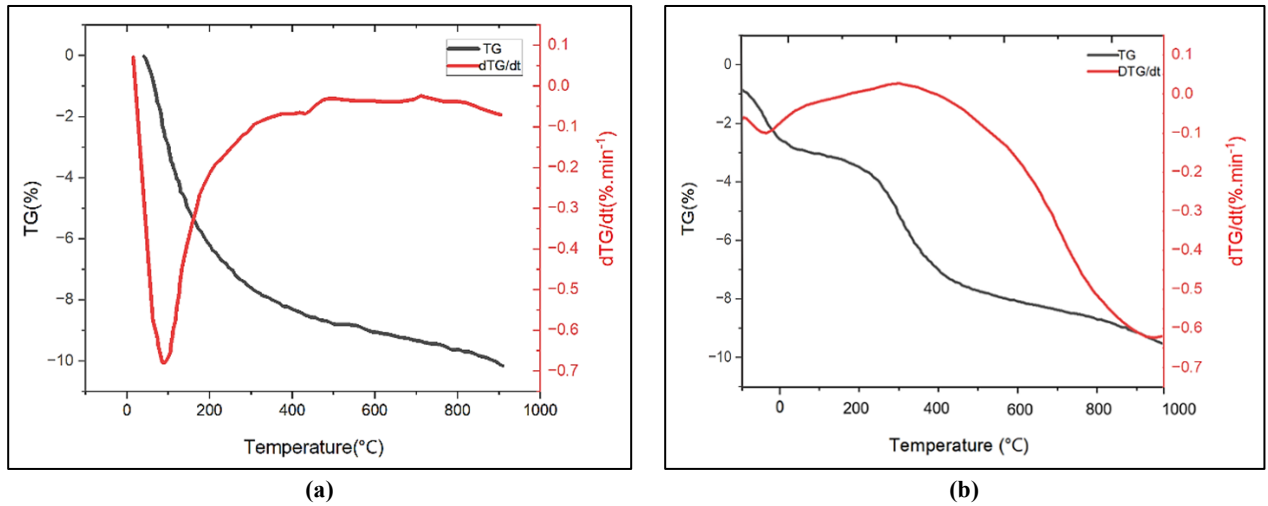


Figure 9: Shows the TGA and DTGA thermograms of prepared HA samples (a) HA₁ and (b) HA₂

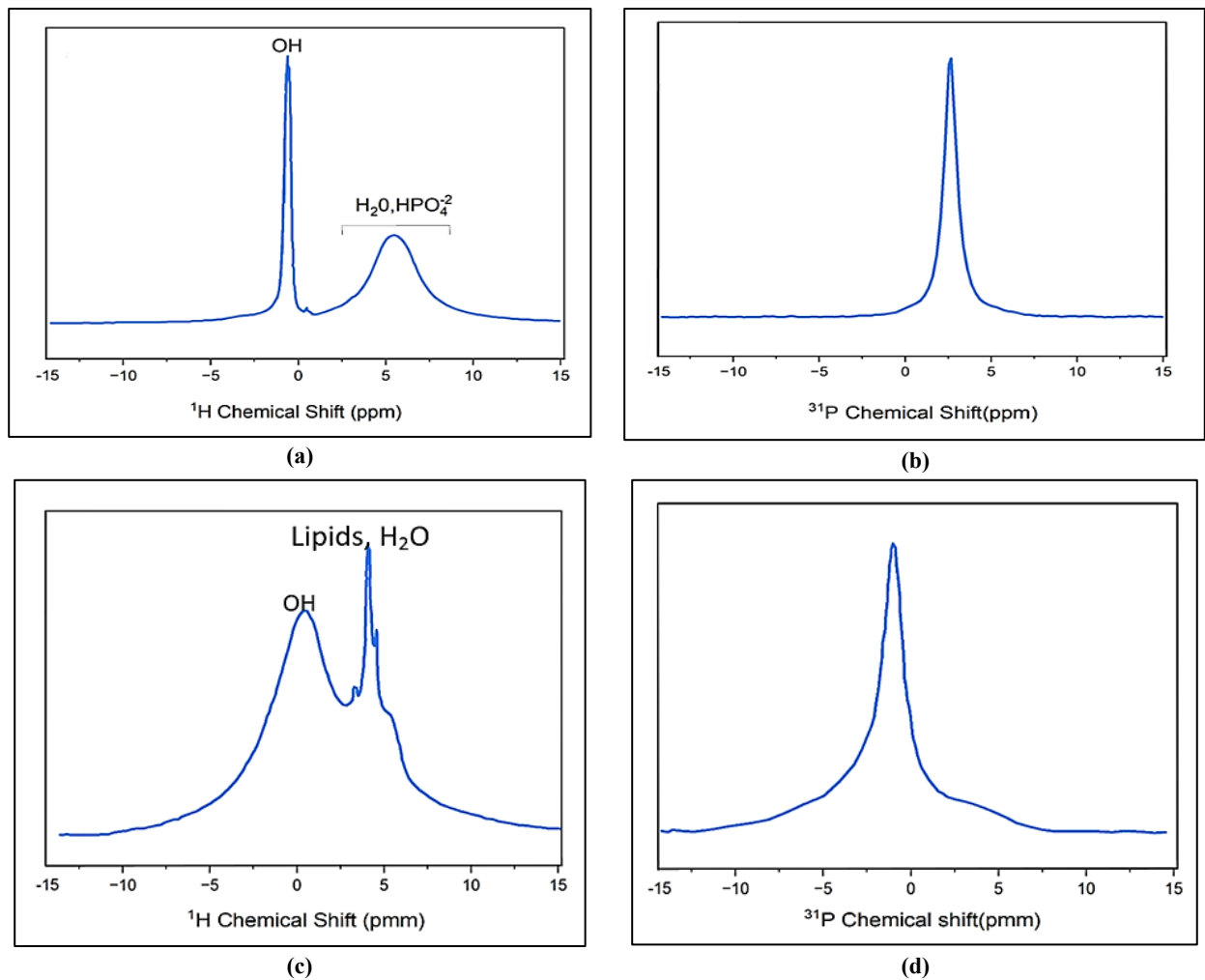


Figure 10: Shows the NMR results for HA₁ (a,b) and HA₂ (c,d)

3.6 FTIR Results

The apatite phase was proven to exist in nano-HA crystals by Fourier transform infrared spectroscopy, as illustrated in Figure 11. The stretching and vibrational modes of OH⁻ ions cause the bands at 3572 cm⁻¹ and 631 cm⁻¹, respectively.

The carbonate bands of Hydroxyapatite derived from bone have an intensity higher than the synthetic Hydroxyapatite. Approximately 1% of carbonates is expected and visible in the synthetics hydroxyapatite due to the synthesis process was done in the air in the presence of CO₂ [22], carbonate was found with 9% percentage in natural hydroxyapatite due to the presence of the organic material from the raw bovine bone [2], which observed in the frequency range from 1550 cm⁻¹ to 1400 cm⁻¹ for ν₃. The bands at 1090 cm⁻¹ and 1040 cm⁻¹ are caused by ν₃ PO₄, the band at 962 cm⁻¹ is caused by ν₁ PO₄, and ν₄ PO₄ causes the bands at 601 cm⁻¹ and 574 cm⁻¹. The 2200 cm⁻¹ to 1950 cm⁻¹ range has a collection of weak intensity bands that result from

overtones and combinations of the ν_1 and ν_3 PO_4 modes. This discovery and the information from TEM suggest that the produced particles are nanomaterials. Wet-precipitated HA has a lot of adsorbed water in the form of physisorbed and chemisorbed water.

After sintering HA_1 & HA_2 at 250°C , as shown in Figure 11 and Figure 12, the broad valleys at 1640 cm^{-1} and $3300\text{--}3570\text{ cm}^{-1}$ (corresponding to H_2O) changed to a plateau. Moreover, the intensity of the peaks owing to CO_3 groups has been reduced. As expected, this indicates that the amount of the carbonate groups was reduced because of their elimination during the heating stroke, as proved by TGA and SDTA analyses. In the case of HA_2 , the intensity of the peaks owing to CO_3 groups has been reduced. This may be due to removing all the organic material from the raw bovine bone and forming HA crystals. The sharpness of the bands shows the well-crystallinity of the sintered nanoparticles. However, regarding HA_1 , the peak attributed to HPO_4 (P-O-H) group in the range $850\text{--}880\text{ cm}^{-1}$ has disappeared because of their conversion to PO_4 .

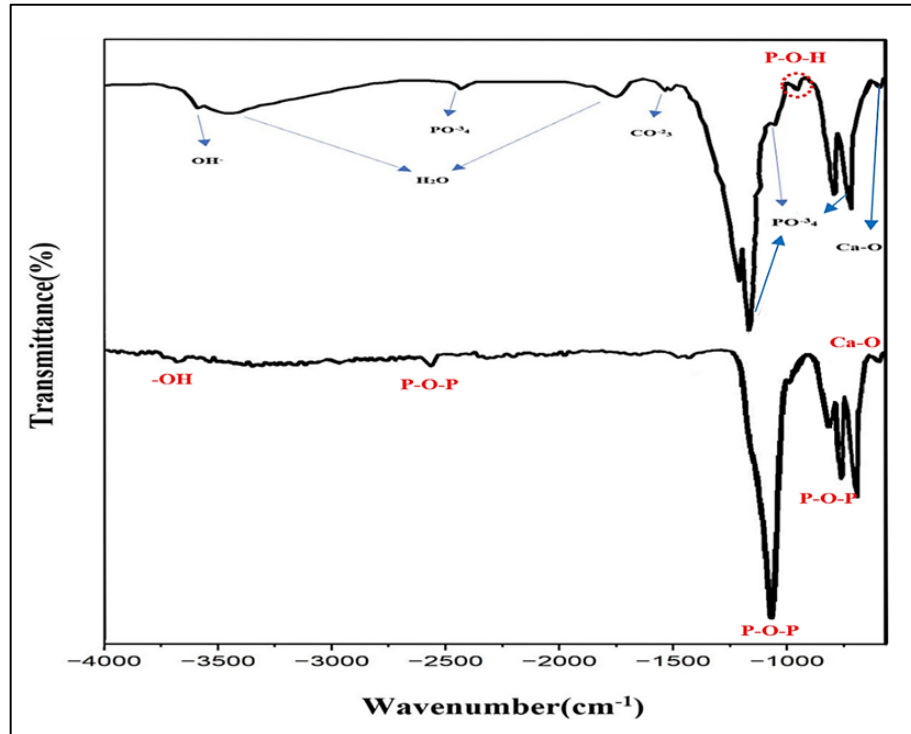


Figure 11: FTIR patterns of Hydroxyapatite (HA_1) before (a) and after (b) cold sintering process

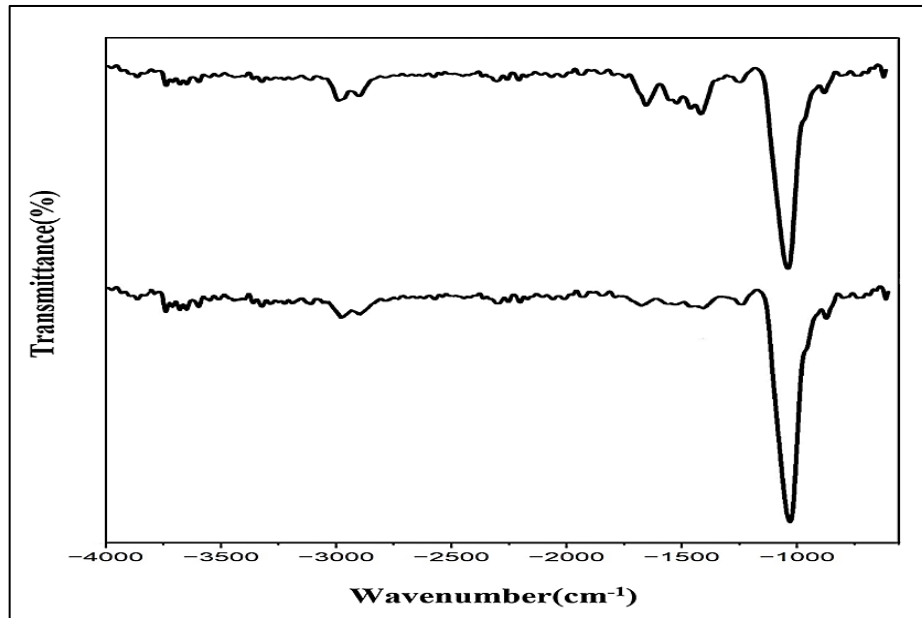


Figure 12: FTIR patterns of Hydroxyapatite (HA_2) before (a) and after (b) cold sintering process

3.7 XRD Results

Figure 13 and 14 show the XRD patterns of the produced HA_1 & HA_2 nanopowders before and after the cold sintering process at different temperatures, revealing apatite production as a single phase with no additional impurity phases. Each pattern matches ICDD Card 00-003-0747. The average crystallite size was determined to be 19 nm 33 nm for HA_1 & HA_2 by using the Scherrer

formula and the (002) plane's full width at half maximum (FWHM) peak, which is independent and doesn't interfere with other peaks. After cold sintering, Some identified peaks got slightly sharper, indicating more excellent particle crystallization of Hydroxyapatite without decomposition to tricalcium phosphate and other phases. Compared with other traditional sintering, the essential advantage of the cold sintering process is that the HA does not decompose during sintering. As the HA₁ crystal sinters, the lattice parameter in the a-axis decreases until it reaches the standardized value ($a = 9.422$ Å in ICDD PDF #54-0022). This phenomenon is significant because it suggests that the HA crystal has undergone structural change following cold sintering. Previous to this, Le Geros et al. [15] revealed that the loss of lattice water caused decreases in the a-axis lattice parameter during continuous heating, as shown in Table 1.

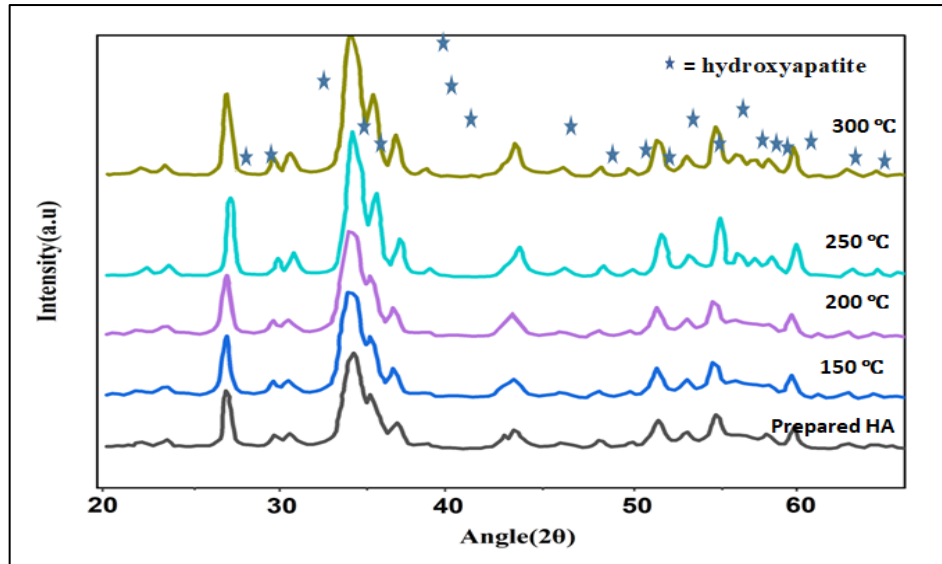


Figure 13: XRD patterns of Hydroxyapatite (HA₁) before (a) and after (b) cold sintering process

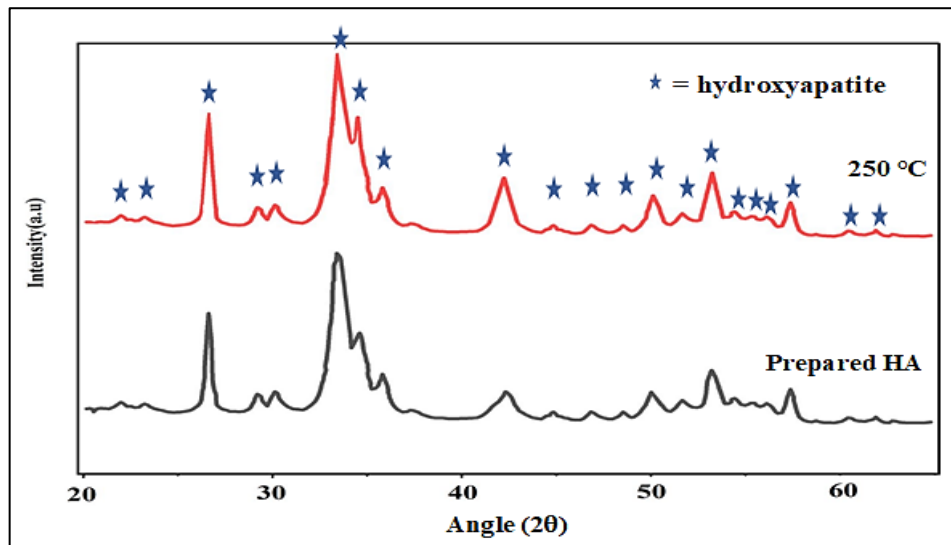


Figure 14: XRD patterns of Hydroxyapatite (HA₂) before (a) and after (b) cold sintering process

Using the Scherrer formula and the full width at half maximum (FWHM) peak corresponding to the (002) plane, which is independent and does not interfere with other peaks, the average crystallite size of starting powder and sintered samples at 200, 250, 300 and 350 were determined to be 19.01, 54, 78, 98 and 116 nm, respectively.

3.8 Sem results of dense HA

The surface morphology and crystal size of the sintered HA₁ & HA₂ were studied under SEM. Figure 15a,b shows SEM images of the HA₁ surface with the highest density, Figure 15c,d shows SEM images of the HA₁ surface with lowest density. It can be easily notice that HA grains have been grown during the sintering process. This study had a 500 MPa uniaxial pressure, 250°C temperature, 10wt.% liquid content and 60 min were ideal for achieving a bulk density of up to 99% for HA₁ and 80 for HA₂. The sintered samples have a grain size more significant than the grain size of the started powder, indicating the good densifications of HA samples. The growth of the grain to this level belongs to the high activity of the nanoparticles due to the increased surface area and the relatively slow heating rate during the sintering process [34-43]. While the sample sintered at 200°C and 100 MPa have the lower densification. This is due to tiny (meso-) pores leaving after evaporation of the trans solvent

in both HA₁ & HA₂ samples. The situation can get worse if insufficient external pressure is applied. The solvent (water) worked well, but the applied force (100 MPa) was insufficient to close the pores [23].

It can be observed that the HA₁ sample has higher densification compared with HA₂ in all environments as shown in Figure 16 a,b. The presence of organic matter in natural Hydroxyapatite HA₂ confirms the FTIR and TGA results, and this organic material will be removed during the cold sintering process, leaving pores that lead to low densification of samples. The calcium to phosphorus molar ratio was calculated using an EDS examination of the HA₁ and HA₂ as shown in Figure 15e and Figure (16 e), respectively. The computed Ca/P ratio was 1.65 for HA₁ and 1.968 for HA₂. This can be done by comparing this ratio with the ideal ratio of 1.667 derived from the chemical formula of HA.

Table 1: The change in the lattice parameters and crystallite size varus temperature

Temperature°C	Lattice parameters		Crystallite Size (nm)
	A,b. Å	C. Å	
HA. Starting powder	9.427	6.889	19.01
200	9.426	6.887	54.79
250	9.424	6.884	78.98
300	9.421	6.882	98.23
350	9.418	6.881	116.6

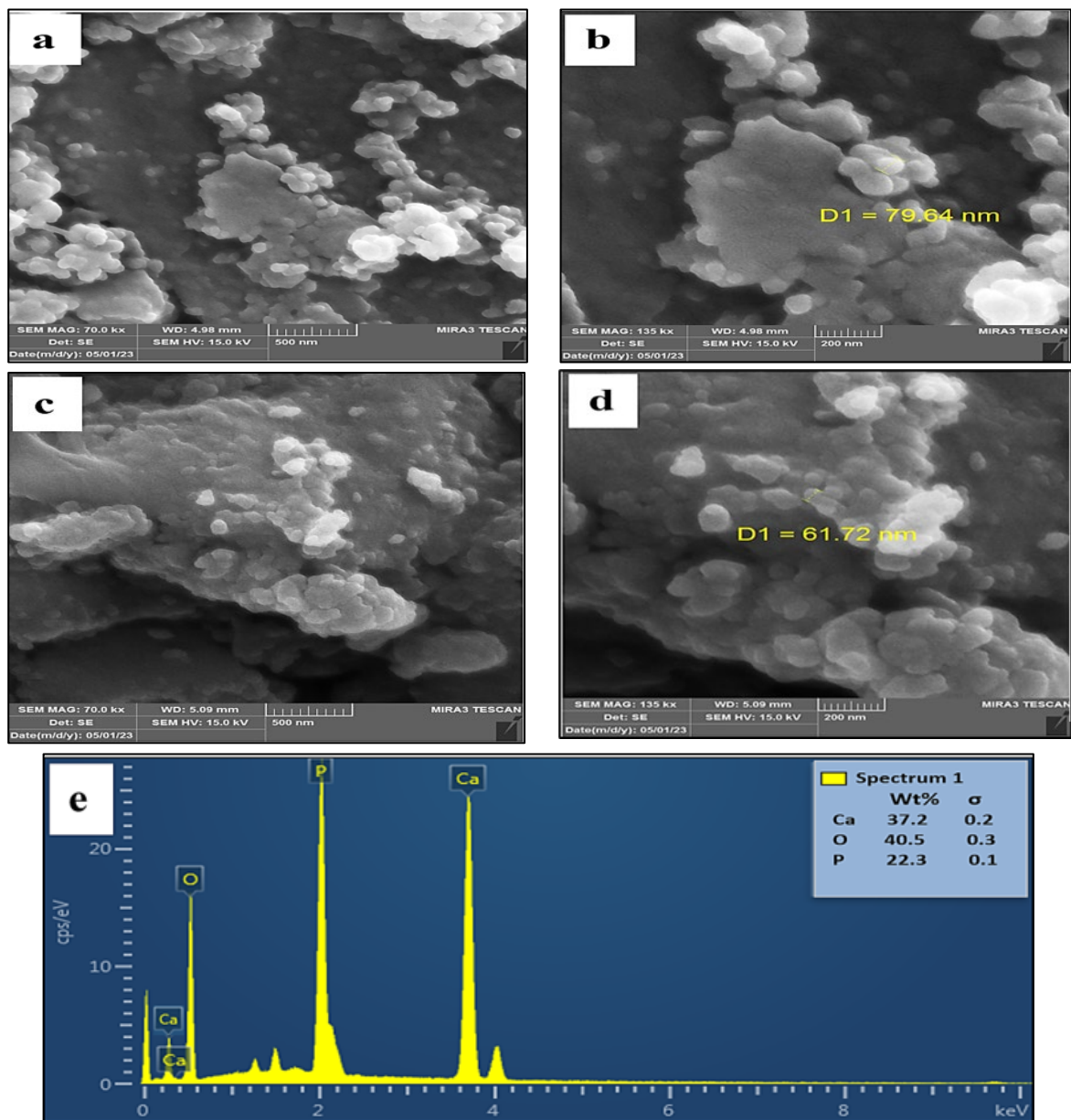


Figure 15: SEM images of the HA₁ surface with highest (a) and lowest density (c). (e) EDS spectra of HA₁ sample

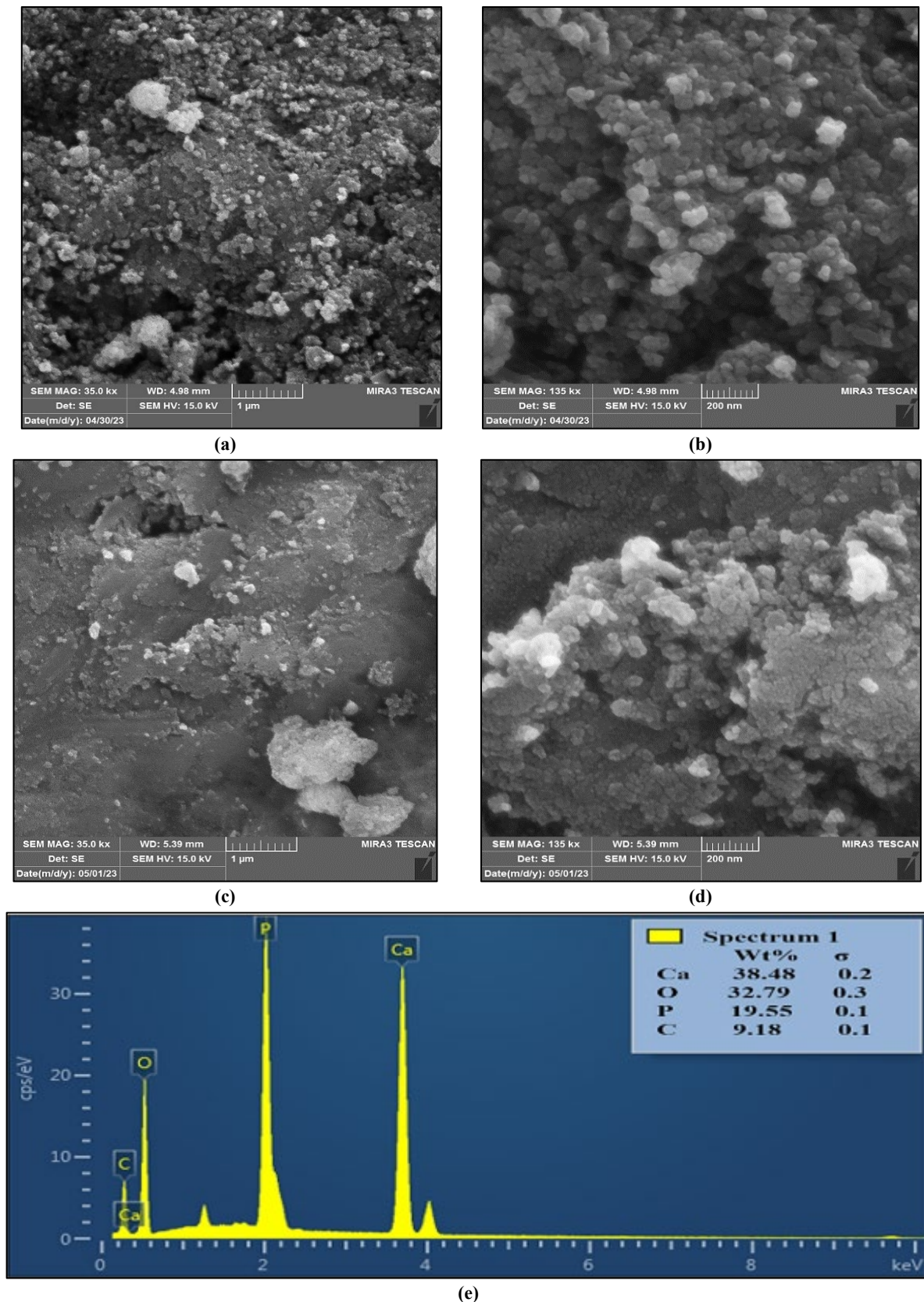


Figure 16: SEM images of the HA₂ surface with highest (a) and lowest density (c). (e) EDS spectra of HA₂

4. Conclusion

In the present work, Hydroxyapatite was prepared using two routes: natural source (Boven bone) and Synthesis by chemical precipitation method. This work aimed to explain the difference between the Cold sintering process of two powders (HA₁ & HA₂). The cold sintering process shows the ability to produce high densification of HA₁ & HA₂. The optimum conditions values that maximize the relative density would be a sintering temperature of 250°C, sintering pressure of 500 MPa, holding time of 60 min, and liquid content of 10 wt.%. Under optimum conditions, the relative density and hardness for HA₁ were 99% and 530 HV,

respectively. The relative density and hardness for HA₂ were 79% and 300 HV, respectively. FTIR and NMR results explain the presence of an amorphous layer of chemisorbed and physisorbed water at the surface of the hydroxyapatite (HA₁&HA₂) crystal. Under 500 MPa applied pressure, during the earliest stages of sintering, the highest densification was achieved by Breaking soft agglomerates of HA particles. The amorphous layer may be trapped between the solid-solid interfaces, which helped the HA particles slide and rearrange. It can be observed that the HA₁ sample has higher densification compared with HA₂ in all environments. The presence of organic matter in natural Hydroxyapatite HA₂ and this organic material will be removed during the cold sintering process, leaving pores that lead to low densification of samples. In summary, a simple and energy-efficient cold sintering process based on low-temperature and high pressure with liquid additives can consolidate hydroxyapatite nanopowder with good performance.

Author contributions

Conceptualization, H. Abbas, H. Smeig and Z. Abdul Ameer; methodology, H. Abbas; validation, H. Smeig; resources, Z. Abdul Ameer; data curation, H. Abbas; writing—original draft preparation, H. Abbas; writing—review and editing, H. Abbas; supervision, H. Smeig. All authors have read and agreed to the published version of the manuscript.

Funding

This research received no specific grant from any funding agency in the public, commercial, or not-for-profit sectors.

Data availability statement

The data that support the findings of this study are available on request from the corresponding author.

Conflicts of interest

The authors declare that there is no conflict of interest.

References

- [1] A. C. Silva, A. H. Aparecida, and F. J. C. Braga, Dispersed hydroxyapatite bioglass 45S5 composites: Comparative evaluation of the use of bovine bone and synthetic hydroxyapatite, *Mater. Sci. Forum*, 727–728 (2012) 1147–1152. <https://doi.org/10.4028/www.scientific.net/MSF.727-728.1147>
- [2] S. Bouyegh, S. Tlili, K. Labiod, M. Hassani, M. Grimet, and O. Bensalem, Preparation and characteristics of synthesized hydroxyapatite from bovine bones and by co-precipitation method, *Int. Conf. Ind. Eng. Oper. Manag.*, 2021.
- [3] E. Neovius and T. Engstrand, Craniofacial reconstruction with bone and biomaterials: Review over the last 11 years, *J. Plast. Reconstr. Aesthetic Surg.*, 63 (2010) 1615–1623. <https://doi.org/10.1016/j.bjps.2009.06.003>
- [4] E. E. Wilson, A. Awonusi, M. D. Morris, D. H. Kohn, M. M. J. Tecklenburg, and L. W. Beck, Three structural roles for water in bone observed by solid-state NMR, *Biophys. J.*, 90 (2006) 3722–3731. <https://doi.org/10.1529%2Fbiophysj.105.070243>
- [5] M. U. Hassan, M. Akmal, and H. J. Ryu, Cold sintering of as-dried nanostructured calcium hydroxyapatite without using additives, *J. Mater. Res. Technol.*, 11 (2021) 811–822. <https://doi.org/10.1016/j.jmrt.2021.01.060>
- [6] D. Grossin et al., Biomimetic apatite sintered at very low temperature by spark plasma sintering: Physico-chemistry and microstructure aspects, *Acta Biomater.*, 6 (2010) 577–585. <https://doi.org/10.1016/j.actbio.2009.08.021>
- [7] H. Guo, A. Baker, J. Guo, and C. A. Randall, Cold Sintering Process: A Novel Technique for Low-Temperature Ceramic Processing of Ferroelectrics, *J. Am. Ceram. Soc.*, 99 (2016) 3489–3507. <https://doi.org/10.1111/jace.14554>
- [8] J. Guo, A. L. Baker, H. Guo, M. Lanagan, and C. A. Randall, Cold sintering process: A new era for ceramic packaging and microwave device development, *J. Am. Ceram. Soc.*, 100 (2017) 669–677. <https://doi.org/10.1111/jace.14603>
- [9] H. Z. Shen, N. Guo, L. Zhao, and P. Shen, Role of ion substitution and lattice water in the densification of cold-sintered hydroxyapatite, *Scr. Mater.*, 177 (2020) 141–145. <https://doi.org/10.1111/jace.14603>
- [10] J. Guo et al., Recent Progress in Applications of the Cold Sintering Process for Ceramic–Polymer Composites, *Adv. Funct. Mater.*, 28 (2018) 1–15. <https://doi.org/10.1002/adfm.201801724>
- [11] X. Zhao et al., Cold sintering ZnO based varistor ceramics with controlled grain growth to realize superior breakdown electric field, *J. Eur. Ceram. Soc.*, 41 (2021) 430–435. <https://doi.org/10.1016/j.jeurceramsoc.2020.09.023>
- [12] S. Grasso et al., A review of cold sintering processes, *Adv. Appl. Ceram.*, 119 (2020) 115–143. <https://doi.org/10.1080/17436753.2019.1706825>
- [13] A. Ndayishimiye et al., Roadmap for densification in cold sintering: Chemical pathways, *Open Ceram.*, 2 (2020) 100019. <https://doi.org/10.1016/j.oceram.2020.100019>
- [14] X. Zhao, J. Guo, K. Wang, T. Herisson De Beauvoir, B. Li, and C. A. Randall, Introducing a ZnO–PTFE (Polymer) Nanocomposite Varistor via the Cold Sintering Process, *Adv. Eng. Mater.*, 20 (2018) 1–8. <https://doi.org/10.1002/adem.201700902>

- [15] M. ul Hassan and H. J. Ryu, Cold sintering and durability of iodate-substituted calcium hydroxyapatite (IO-HAp) for the immobilization of radioiodine, *J. Nucl. Mater.*, 514 (2019) 84–89. <https://doi.org/10.1016/j.jnucmat.2018.11.024>
- [16] J. Guo, S. S. Berbano, H. Guo, A. L. Baker, M. T. Lanagan, and C. A. Randall, Cold Sintering Process of Composites: Bridging the Processing Temperature Gap of Ceramic and Polymer Materials, *Adv. Funct. Mater.*, 26 (2016) 7115–7121. <https://doi.org/10.1002/adfm.201602489>
- [17] M. Si et al., Preparation of zinc oxide/poly-ether-ether-ketone (PEEK) composites via the cold sintering process, *Acta Mater.*, 215 (2021) 117036. <https://doi.org/10.1016/j.actamat.2021.117036>
- [18] A. Ndayishimiye, Z. A. Grady, K. Tsuji, K. Wang, S. H. Bang, and C. A. Randall, Thermosetting polymers in cold sintering: The fabrication of ZnO-polydimethylsiloxane composites, *J. Am. Ceram. Soc.*, 103 (2020) 3039–3050. <https://doi.org/10.1111/jace.17009>
- [19] J. Dong, M. Kermani, C. Hu, and S. Grasso, Flash cold sintering of Nb2O5: polarity and electrolyte effects, *J. Asian Ceram. Soc.*, 9 (2021) 934–939. <https://doi.org/10.1080/21870764.2021.1926704>
- [20] V. Medri, F. Servadei, R. Bendoni, A. Natali Murri, A. Vaccari, and E. Landi, Nano-to-macroporous TiO₂ (anatase) by cold sintering process, *J. Eur. Ceram. Soc.*, 39 (2019) 2453–2462. <https://doi.org/10.1016/j.jeurceramsoc.2019.02.047>
- [21] J. Cockburn and R. Boston, Cold sintering of YBa₂Cu₃O_{7- δ} , *RSC Adv.*, 9 (2019) 40917–40923. <https://doi.org/10.1039/c9ra08744c>
- [22] T. Hérisson de Beauvoir, K. Tsuji, X. Zhao, J. Guo, and C. Randall, Cold sintering of ZnO-PTFE: Utilizing polymer phase to promote ceramic anisotropic grain growth, *Acta Mater.*, 186 (2020) 511–516. <https://doi.org/10.1016/j.actamat.2020.01.002>
- [23] S. Iqbal, M. ul Hassan, H. J. Ryu, and J. Il Yun, Efficient immobilization of ionic corrosion products by a silica-hydroxyapatite composite: Via a cold sintering route, *RSC Adv.*, 9 (2019) 34872–34879. <https://doi.org/10.1039/c9ra04280f>
- [24] S. J. Gregg and K. S. W. Sing, Adsorption, surface area and porosity: Second edition. (1982)1-313. *AdvancedMaterialsThermodynamics*, S. J. Gregg, Kenneth S.W. Sing - Adsorption, surface area, and porosity-Academic Press .
- [25] J. Reyes-Gasga et al., Structural and thermal behaviour of human tooth and three synthetic hydroxyapatites from 20 to 600 °C, *J. Phys. D: Appl. Phys.*, 41 (2008). <https://doi.org/10.1088/0022-3727/41/22/225407>
- [26] G. Burks, F. H. Dill, and M. I. Nathan, The Effect of Temperature on the Properties of GaAs Laser, *Proc. IEEE*, 51 (1963) 947–948. <https://doi.org/10.1109/PROC.1963.2345>
- [27] I. Ho et al., Effects of pH and reaction temperature on hydroxyapatite powders synthesized by precipitation, *J. Korean Ceram. Soc.*, no. 0123456789, 2019. <https://doi.org/10.1007/s43207-019-00004-0>
- [28] N. Vandecandelaere, C. Rey, and C. Drouet, Biomimetic apatite-based biomaterials: On the critical impact of synthesis and post-synthesis parameters, *J. Mater. Sci. Mater. Med.*, 23 (2012) 2593–2606. <https://doi.org/10.1007/s10856-012-4719-y>
- [29] C. Jäger, T. Welzel, W. Meyer-Zaika, and M. Epple, A solid-state NMR investigation of the structure of nanocrystalline hydroxyapatite, *Magn. Reson. Chem.*, 44 (2006) 573–580. <https://doi.org/10.1002/mrc.1774>
- [30] Y. Wang et al., Water-mediated structuring of bone apatite, *Nat. Mater.*, 12 (2013) 1144–1153. <https://doi.org/10.1038/nmat3787>
- [31] E. E. Wilson, A. Awonusi, M. D. Morris, D. H. Kohn, M. M. J. Tecklenburg, and L. W. Beck, Highly ordered interstitial water observed in bone by nuclear magnetic resonance, *J. Bone Miner. Res.*, 20 (2005) 625–634. <https://doi.org/10.1359/JBMR.041217>
- [32] A. Kafilak and W. Kolodziejski, Phosphorus-31 spin-lattice NMR relaxation in bone apatite and its mineral standards, *Solid State Nucl. Magn. Reson.*, 31 (2007) 174–183. <https://doi.org/10.1016/j.ssnmr.2007.04.005>
- [33] A. A. Gaidash, L. N. Sinitsa, O. A. Babenko, and A. A. Lugovskoy, Nanoporous Structure of Bone Matrix at Osteoporosis from Data of Atomic Force Microscopy and IR Spectroscopy, *J. Osteoporos.* (2011) 1–7. <https://doi.org/10.4061/2011/162041>
- [34] I. Z.J. Kadhim, F.J. Al-Hasani, E.S. Al-hassani, Investigation the bioactivity of cordierite/hydroxyapatite ceramic material used in bone regeneration. *SILICON* 15 (2023) 6673–6682.
- [35] G. Montel, G. Bonel, J. C. Heughebaert, J. C. Trombe, and C. Rey, New concepts in the composition, crystallization and growth of the mineral component of calcified tissues, *J. Cryst. Growth*, 53 (1981) 74–99. [https://doi.org/10.1016/0022-0248\(81\)90057-9](https://doi.org/10.1016/0022-0248(81)90057-9)
- [36] S. S. A. Abidi and Q. Murtaza, Synthesis and characterization of nano-hydroxyapatite powder using wet chemical precipitation reaction, *J. Mater. Sci. Technol.*, 30 (2014) 307–310. <https://doi.org/10.1016/j.jmst.2013.10.011>

- [37] Z. Shen and M. Nygren, Microstructural prototyping of ceramics by kinetic engineering: Applications of spark plasma sintering, *Chem. Rec.*, 5 (2005) 173–184. <https://doi.org/10.1002/tcr.20043>
- [38] M. Ibrahim, M. Labaki, J. M. Giraudon, and J. F. Lamonier, Hydroxyapatite, a multifunctional material for air, water and soil pollution control: A review, *J. Hazard. Mater.*, 383 (2020) 121139. <https://doi.org/10.1016/j.jhazmat.2019.121139>
- [39] I. Akin and G. Goller, Handbook of Bioceramics and Biocomposites, *Handb. Bioceram. Biocomposites.*, 2014. <https://doi.org/10.1007/978-3-319-09230-0>
- [40] S. Mondal et al., Physico-chemical characterization and biological response of Labeo rohita-derived hydroxyapatite scaffold, *Bioprocess Biosyst. Eng.*, 37 (2014) 1233–1240. <https://doi.org/10.1007/s00449-013-1095-z>
- [41] Q.A. Hamad, F.J. Al-Hasani, N.K. Faheed, Comparative study of biotin and hydroxyapatite on biological properties of composite coating, *Int J Biomater.*, 2022 (2022) 1-11. <https://doi.org/10.1155/2022/8802111>
- [42] Z.J. Kadhim, F.J. Mohammed, E.S. Al-hassani, Effect of cordierite additions on mechanical properties of hydroxyapatite used in medical applications, *Eng Technol J.*, 41(2023) 807–821. <https://doi.org/10.30684/etj.2023.138142.1375>
- [43] Q. A. Hamad, H. A. Al-kaisy, M. N. Al-shroofy, and N. K. Faheed, Evaluation of Novel Chitosan Based Composites Coating on Wettability for Pure Titanium Implants, *J. Renew Mater.*, 11(2023)1601-1612. <https://doi.org/10.32604/jrm.2023.023213>